Fully Constrained Linear Subpixel Classification Algorithms: A Comparative Analysis Based on Heuristic

Uttam Kumar, *Member, IAENG*, Sangram Ganguly, Cristina Milesi, and Ramakrishna R. Nemani

***Abstract*—During the past two and a half decades, many subpixel classification algorithms have been developed to classify multispectral and hyperspectral data for spatio-temporal data mining. The aim of these classification algorithms is to disintegrate a pixel spectrum into its constituent spectra through a mixture model assuming that observed data are linear mixtures of two or more objects, representing a mixed pixel. The linear mixture model allows the presence of a number of target classes with the fractions of their fixed spectrum corresponding to the area occupied by that class in a pixel. The linear model is inverted to produce estimates of those fractional abundances. All of these algorithms are either unconstrained or partially constrained or fully constrained depending on whether the abundance non-negativity and abundance sum-to-one constraints are imposed. More often, the constrained algorithms are appropriate for target class quantification and abundance fraction estimation. In this paper, we perform a comparative analysis of five state of the art fully constrained linear subpixel classification algorithms – fully constrained least squares (FCLS), modified FCLS (MFCLS), simplex projection unmixing (SPU), constrained sparse unmixing via variable splitting and augmented Lagrangian (CSUnSAL) and CSUnSAL Total Variation (CSUnSAL TV). The algorithms were tested on computer-simulated data of various signal to noise ratio and Landsat-5 TM data of an agricultural landscape and an urban scenario. The results were validated using descriptive statistics, correlation coefficient, RMSE and probability of success.**

***Index Terms*—algorithm, constrained model, endmember, linear spectral mixture, mixed pixel**

I. Introduction

LINEAR spectral mixture analysis has remained an important area of active research to characterize the mixed pixels in medium to coarse spatial resolution remote sensing (RS) data [1]. It employs a linear mixture model (LMM) that infers a set of pure spectral signatures (endmembers), and fractions of these endmembers (abundances) in each pixel of the image [2]. LMM assumes that the spectra collected by imaging instrument are a linear combination of endmembers, weighted by their corresponding abundances. The endmembers are either derived using some endmember extraction algorithms [3], [4] from the image pixels or obtained from an endmember library available *a priori*. Once the endmembers are known, LMM is inverted to produce estimates of those fractional abundances, i.e. the model allows a number of target materials to be present, each contributing a fraction of its spectrum corresponding to the area occupied by that category in a pixel. Numerous approaches have been proposed in the past two and a half decades to solve the mixed pixel problem for a wide variety of applications ranging from modeling the component mixtures to solving the linear combinations to obtain abundances through geometrical, statistical and sparse regression-based approaches [5]-[7]. The discussion on this topic can be continued till *ad nauseum* [8]. The optimal solution of these models can be unconstrained, partially constrained or fully constrained (when the abundance non-negativity constraint (ANC) and abundance sum-to-one constraint (ASC) are imposed). ANC restricts the abundance values from being negative and ASC confines the sum of abundance values of all the classes to unity. Although unconstrained and partially constrained algorithms are appropriate for applications seeking target detection, identification and discrimination, constrained models are more suitable for target quantification and for estimating abundance fractions. Undoubtedly, the abundance maps obtained from fully constrained models render more accurate fractional estimates of each class compared to per-pixel classification.

In this paper, we perform a comparative analysis of five different state of the art fully constrained unmixing algorithms namely, fully constrained least squares (FCLS), modified FCLS (MFCLS), simplex projection unmixing (SPU), constrained sparse unmixing via variable splitting and augmented Lagrangian (CSUnSAL) and CSUnSAL Total Variation (CSUnSAL TV) based on heuristic. The algorithms are first tested on computer simulated noise-free and noisy data of different signal to noise ratio. Subsequently, Gaussian noise (a random variable with 0 mean and fixed variance) was induced in the data to judge the robustness of the algorithms. In the second and third set of experiments with the real world data, 11 Landsat-5 TM scenes (of 30 m spatial resolution) of an agricultural landscape (near Fresno, California, USA), and a Landsat scene of an urban scenario (San Francisco, California, USA) were used to evaluate the algorithms. These data were

Manuscript received July 9, 2015. This work was supported by Oak Ridge Associated Universities (ORAU), TN, USA as part of the NASA Postdoctoral Program (NPP).

Uttam Kumar is a NPP Fellow with the NASA Ames Research Center, Moffett Field, CA 94035, USA (phone: 650-604-1542; e-mail: uttam.kumar@ nasa.gov).

Sangram Ganguly is with BAERI / NASA Ames Research Center, Moffett Field, CA 94035, USA (e-mail: sangram.ganguly@nasa.gov).

Cristina Milesi and Ramakrishna R. Nemani are with the NASA Ames Research Center, Moffett Field, CA 94035, USA (e-mail: cristina.milesi@gmail.com, rama.nemani@nasa.gov).

ISBN: 978-988-14047-2-5
ISSN: 2078-0958 (Print); ISSN: 2078-0966 (Online)

analyzed by deriving vegetation, substrate and dark objects (shadows, deep water) endmember fractions with respect to the ground measurements for the agricultural area and by comparing with the high-resolution World View-2 (WV-2) (of 2 m spatial resolution) unmixed image for the urban area respectively. The results were evaluated and the sources of errors were analyzed using descriptive statistics, Pearson product-moment correlation coefficient (cc), root mean square error (RMSE) and probability of success. The paper is organized as follows: section II discusses the general principle of linear mixture model, section III discusses algorithms for fully constrained linear mixture models and section IV details the data used in this analysis. Results and discussion are presented in section V.

II. Linear Mixture Model (LMM)

If there are M spectral bands and N classes, then associated with each pixel is a M-dimensional vector $\mathbf{y}$ whose components are the gray values corresponding to the M bands. Let $\mathbf{E} = [e_1, \ldots e_{n-1}, e_n, e_{n+1} \ldots, e_N]$ be a $M \times N$ matrix, where $\{e_n\}$ is a column vector representing the spectral signature (endmember) of the nth target material. For a given pixel, the abundance or fraction of the nth target material present in the pixel is denoted by α_n, and these values are the components of the N-dimensional abundance vector $\boldsymbol{\alpha}$. Assuming LMM [9], the spectral response of a pixel in any given spectral band is a linear combination of all the endmembers present in the pixel at the respective spectral band. For each pixel, the observation vector $\mathbf{y}$ is related to $\mathbf{E}$ by a linear model written as

$$\mathbf{y} = \mathbf{E}\boldsymbol{\alpha} + \boldsymbol{\eta} \tag{1}$$

where $\boldsymbol{\eta}$ accounts for the measurement noise. We further assume that the components of the noise vector $\boldsymbol{\eta}$ are zero-mean random variables that are i.i.d. (independent and identically distributed). Therefore, covariance matrix of the noise vector is $\sigma^2\mathbf{I}$, where σ^2 is the variance, and $\mathbf{I}$ is $M \times M$ identity matrix.

III. Constrained Mixture Models

The conventional approach to extract the abundance values is to minimize $\|\mathbf{y} - \mathbf{E}\boldsymbol{\alpha}\|$ as in (2):

$$\boldsymbol{\alpha}_{\text{UCLS}} = (\mathbf{E}^T\mathbf{E})^{-1}\mathbf{E}^T\mathbf{y} \tag{2}$$

which is termed as unconstrained least squares (UCLS) estimate of the abundance. The value of α_n is the abundance of the nth class in an abundance map. If no constraints are imposed on the abundances, the estimated abundance fractions may deviate with a wide range. To avoid such conditions, generally two constraints are imposed on the model in (1): the abundance non-negativity constraint (ANC) given as (3) and the abundance sum-to-one constraint (ASC) expressed as (4)

$$\alpha_n \geq 0 \; \forall \; n: 1 \leq n \leq N \tag{3}$$

and

$$\textstyle\sum_{n=1}^{N} \alpha_n = 1. \tag{4}$$

ANC and ASC allows the value of abundance in any given pixel to range between 0 to 1, where 0 indicates absence of a particular class and 1 indicates presence of only that class in a pixel. Intermediate values between 0 and 1 represent a fraction of that class. When only ASC is imposed on the solution, the sum-to-one constrained least squares (SCLS) estimate of the abundance is obtained by

$$\boldsymbol{\alpha}_{\text{SCLS}} = \mathbf{E}^T\mathbf{E}^{-1}\left(\mathbf{E}^T\mathbf{y} - \frac{\lambda}{2}1\right) \tag{5}$$

where

$$\lambda = \frac{2(\mathbf{1}^T(\mathbf{E}^T\mathbf{E})^{-1}\,\mathbf{E}^T\mathbf{y}-\mathbf{1})}{\mathbf{1}^T(\mathbf{E}^T\mathbf{E})^{-1}\mathbf{1}}. \tag{6}$$

The SCLS solution may have negative abundance values but they add to unity. With this background, next we discuss five state of the art fully constrained linear mixture models.

A. Fully Constrained Least Squares (FCLS)

FCLS [7] extends NNLS (Nonnegative Least Squares) algorithm [10] to minimize $\|\mathbf{E}\boldsymbol{\alpha} - \mathbf{y}\|$ subject to $\boldsymbol{\alpha} \geq 0$ by including ASC. ASC is included in the signature matrix $\mathbf{E}$ by a new signature matrix ($\mathbf{SME}$) defined by

$$\mathbf{SME} = \begin{bmatrix} \theta\mathbf{E} \\ \mathbf{1}^T \end{bmatrix} \tag{7}$$

with $\mathbf{1} = (\underbrace{11111..1}_{N})^T$, and

$$\mathbf{s} = \begin{bmatrix} \theta\mathbf{y} \\ 1 \end{bmatrix}. \tag{8}$$

θ in (7) and (8) regulates ASC. Using these two equations an FCLS algorithm can be derived directly from the NNLS algorithm by replacing signature matrix $\mathbf{E}$ with $\mathbf{SME}$ and pixel vector $\mathbf{y}$ with $\mathbf{s}$. For a detailed derivation of the NNLS algorithm, readers are requested to refer (Lawson and Hanson, 1995) [10].

B. Modified Fully Constrained Least Squares (MFCLS)

ANC is a major problem in solving constrained linear unmixing problems as it forbids use of Lagrange multiplier. Chang (2003) [7] proposed the replacement of $\alpha_n \geq 0 \; \forall \; n: 1 \leq n \leq N$ with absolute ASC (AASC), $\sum_{n=1}^{N}|\alpha_n| = 1$. AASC allows usage of Lagrange multiplier along with exclusion of negative abundance fractions leading to optimal constrained least squares solution satisfying both ASC and AASC with all nonnegative fractions. This method is called MFCLS, expressed as

$$\min_{\alpha\in\Delta}\{(\mathbf{y} - \mathbf{E}\boldsymbol{\alpha})(\mathbf{y} - \mathbf{E}\boldsymbol{\alpha})^T\} \tag{9}$$

subject to $\Delta=\{\alpha|\sum_{n=1}^{N}\alpha_n = 1 \text{ and } \sum_{n=1}^{N}|\alpha_n| = 1\}$.

It turns out that the solution to (9) is

$$\hat{\alpha}_{\text{MFCLS}} = \hat{\alpha}_{\text{UCLS}} - (\mathbf{E}^T\mathbf{E})^{-1}[\lambda_1\mathbf{1} + \lambda_2 sign(\alpha)] \tag{10}$$

where $\hat{\alpha}_{\text{UCLS}} = (\mathbf{E}^T\mathbf{E})^{-1}\,\mathbf{E}^T\mathbf{y}$ which is the unconstrained solution as in (2). The ASC and the AASC constraints are now used to compute λ_1 and λ_2 by replacing α with $\hat{\alpha}_{\text{UCLS}}$ with the following constraints: $\sum_{n=1}^{N}\alpha_n = 1^T\alpha = 1$, and

ISBN: 978-988-14047-2-5
ISSN: 2078-0958 (Print); ISSN: 2078-0966 (Online)

$\sum_{n=1}^{N}|\alpha_n| = sign\ (\alpha)^T\alpha = 1,$
where $sign\ (\alpha) = (\omega_1, \omega_2, \ldots \omega_{n-1}, \omega_n, \omega_{n+1} \ldots \omega_N)^T$ and

$$\omega_n = \begin{cases} \frac{\alpha_n}{|\alpha_n|}; \text{ if } \alpha_n \neq 0 \\ 0; \text{ if } \alpha_n = 0 \end{cases}$$

The MFCLS algorithm is briefly stated as

Step 1: Set $\hat{\alpha}_{\text{MFCLS}} = \hat{\alpha}_{\text{SCLS}}$ from (5).
Step 2: Compute λ_1 and λ_2
Step 3: Compute $\hat{\alpha}_{\text{MFCLS}} = \hat{\alpha}_{\text{SCLS}} - (\mathbf{E}^T\mathbf{E})^{-1}[\lambda_1\mathbf{1} + \lambda_2 sign(\alpha)]$
Step 4: If $\hat{\alpha}_{\text{MFCLS}}$ has any negative value, go to step 2 else exit.

MFCLS algorithm utilizes the SCLS solution. Step 4 terminates the algorithm when all the components are nonnegative. Alternatively, a preselected threshold can be used for a fast implementation. For a more detailed derivation, readers are directed to refer [7], pp. 184.

C. Simplex Projection Unmixing (SPU)

SPU [11] is a supervised unmixing algorithm, equivalent to FCLS. SPU finds the projection of a point onto a generic simplex and minimizes the least squares error while imposing ANC and ASC. It greatly reduces the computational complexity without following any optimization or maximization, while recursively reducing the dimensionality of the problem to obtain a suitable abundance vector. At each run, the algorithm identifies an endmember that has zero abundance and orthogonally projects on a hyperplane of a dimension less than the previous one. The simplex projection algorithm (simplex_project) is briefed below. For a more detailed derivation, readers are requested to refer [11].

Consider a data set of P points $\mathbf{y}_p \in \mathbb{R}^M, p = 1 \ldots P$, and N endmembers $\{e_1, \ldots e_{n-1}, e_n, e_{n+1} \ldots, e_N\}$. The goal is to project all points $\mathbf{y}_p$ on to a simplex S_I spanned by the N endmembers in the set $I = \{e_1, \ldots e_{n-1}, e_n, e_{n+1} \ldots, e_N\}$ producing projected points $\mathbf{y'}_p$ and corresponding abundance vectors $\hat{\boldsymbol{\alpha}}_p = (\alpha_{p1}, \ldots, \alpha_{pN})$. The projected points $\mathbf{y'}_p$ are determined through $\mathbf{y'}_p = \mathbf{E}\hat{\boldsymbol{\alpha}}_p$.

Input → $\mathbf{y}, \mathbf{E}$ where $\mathbf{y}$ is a M x P matrix, the points to unmix and $\mathbf{E}$ is a M x N matrix, the N endmembers (or classes).

Output → $\boldsymbol{\alpha}$ where $\boldsymbol{\alpha}$ is a N x P vector.
start
If $N = 1$ then $\boldsymbol{\alpha} = \bar{1}$; return;
$I = \{\}$;
for $\forall\ p \in [1, \ldots, P]$, calculate partial abundance

$$\mathbf{par\_abn}^p = \left(\hat{\mathbf{E}}^T\hat{\mathbf{E}}\right)^{-1}\hat{\mathbf{E}}^T(\mathbf{y} - e_1).$$

If $\forall\ j: par\_abn_j^p \geq 0$ and $\sum_j par\_abn_j^p \leq 1$ then
$\boldsymbol{\alpha}_p = [1 - \sum_j par\_abn_j^p,\ \mathbf{par\_abn}^p]$;
else
project $\mathbf{y}_p$ onto simplex plane with $\hat{\mathbf{E}}\left(\hat{\mathbf{E}}^T\hat{\mathbf{E}}\right)^{-1}\hat{\mathbf{E}}^T(\mathbf{y} - e_1) + e_1$
Add p to I;
Calculate endmember distance matrix D;
for $\forall\ i \in [1, \ldots, N]$,
Calculate volume V_i of subbsimplex $\mathbf{E}_i = [e_1, \ldots e_{i-1}, e_{i+1} \ldots, e_N]$ using $(-1)^N 2^{N-1}((\mathrm{N}-1)!)^2 V^2 = \det(\boldsymbol{C}_{1,2,\ldots N})$
where $\boldsymbol{C}_{1,2,\ldots N} = \begin{pmatrix} \boldsymbol{D}_{1,2,\ldots N} & \mathbf{1} \\ \mathbf{1} & 0 \end{pmatrix}$, with $\boldsymbol{D}_{1,2,\ldots N} = \left[d_{i,j}^2\right]_{i,j=1,2,\ldots N}$.
Calculate the incenter $\boldsymbol{c}$: $\alpha_i^c = \mathrm{V}_i / \sum_{i=1}^{N} \mathrm{V}_i$ & $\boldsymbol{c} = \mathbf{E}\boldsymbol{\alpha}^c$
for $\forall\ i \in [1, \ldots, N]$
$I = \{\}$;
for $\forall\ j \in I$
Solve $\mathbf{y}_j = \mathbf{E}_i^c\mathbf{b}^i$ for $\mathbf{b}^i$;
if $\forall\ k$: $\mathbf{b}_k^i \geq 0$ then
Add j to I_i;
if $i \neq \{\}$ then
$\boldsymbol{\alpha}^r = \text{simplex\_project}(\mathbf{y}_{Ii}, \mathbf{E}_i)$;
$\boldsymbol{\alpha}([1, \ldots, i-1, i+1, \ldots N], I_i) = \boldsymbol{\alpha}^r$;
$\boldsymbol{\alpha}(i, I_i) = \bar{0}$;
end

D. Constrained Sparse unmixing via variable splitting and augmented Lagrangian (CSUnSAL)

Sparse regression [12] is a new direction in unmixing which is related to both statistical and geometrical frameworks. Endmember search is conducted in a large library, say $\mathbf{E} \in \mathbb{R}^{M \times N}$, where $M < N$ and $\boldsymbol{\alpha} \in \mathbb{R}^N$. It is possible that only a few signatures contained in $\mathbf{E}$ would involve in the mixed pixel spectrum. Therefore, $\boldsymbol{\alpha}$ will contain many values of zero and is a sparse vector. The sparse regression problem is expressed as

$$\min_{\boldsymbol{\alpha}} \|\boldsymbol{\alpha}\|_0 \quad \text{subject to} \quad \|\mathbf{y} - \mathbf{E}\boldsymbol{\alpha}\|_2 \leq \delta, \quad \boldsymbol{\alpha} \geq 0,\ \mathbf{1}^T\boldsymbol{\alpha} = 1 \qquad (11)$$

where $\|\boldsymbol{\alpha}\|_0$ denotes the number of nonzero components of $\boldsymbol{\alpha}$, and $\delta \geq 0$ is the noise and modeling error tolerance. A set of sparsest signals belonging to the (N-1) probability simplex satisfying error tolerance inequality defines the solution of (11). When the fractional abundances from sparse regression follow ANC and ASC, the problem is referred to as constrained sparse regression (CSR). The general CSR problem is given by (12).

$$\min_{\boldsymbol{\alpha}} (1/2)\|\mathbf{E}\boldsymbol{\alpha} - \mathbf{y}\|_2^2 + \lambda\|\boldsymbol{\alpha}\|_1 \qquad (12)$$
$$\text{subject to:} \quad \boldsymbol{\alpha} \geq 0,\ \mathbf{1}^T\boldsymbol{\alpha} = 1$$

where $\|\boldsymbol{\alpha}\|_2$ and $\|\boldsymbol{\alpha}\|_1$ are the l_2 and l_1 norms and $\lambda \geq 0$ is a weighing factor between the l_2 and l_1 terms. SUnSAL is based on the alternating direction method of multipliers (ADMM) [13], [14]. ADMM can be derived as a variable splitting procedure followed by the adoption of an augmented Lagrangian method to solve the constrained problem. The algorithm is briefly stated here, readers are encouraged to refer [15] for detailed derivation. Assume that $\mathbf{E}$ is known and corresponds to underdetermined systems ($N > M$) rather than obtained from an endmember extraction algorithm (where $N < M$). Consider arbitrary $\mu > 0$, $\mathbf{u}_0, \mathbf{d}_0 \in \mathbb{R}^{aff\_dim}$ (where *aff_dim* is an affine dimension), and $\{\boldsymbol{\alpha}_i \in \mathbb{R}^N, \mathbf{u}_i, \mathbf{d}_i \in \mathbb{R}^{aff\_dim}$, where $i = 0, 1, \ldots\}$.
Step 1: Let $i = 0$, select $\mu > 0$, $\mathbf{u}_0$, $\mathbf{d}_0$

ISBN: 978-988-14047-2-5
ISSN: 2078-0958 (Print); ISSN: 2078-0966 (Online)

Step 2: Continue step 3 to step 8 until specified condition is achieved.
Step 3: Compute $\mathbf{w} = \mathbf{E}^T\mathbf{y} + \mu(\mathbf{u}_i + \mathbf{d}_i)$
Step 4: Compute $\boldsymbol{\alpha}_{i+1} = \mathbf{B}^{-1}\mathbf{w} - \mathbf{C}\,(1^T\mathbf{B}^{-1}\mathbf{w} - 1)$
Step 5: Compute $\mathbf{v}_i = \boldsymbol{\alpha}_{i+1} - \mathbf{d}_i$
Step 6: Compute $\mathbf{u}_{i+1} = \max\{0, \text{soft}\left(\mathbf{v}_i, {}^{\lambda}/_{\mu}\right)\}$
Step 7: Compute $\mathbf{d}_{i+1} = \mathbf{d}_i - (\boldsymbol{\alpha}_{i+1} - \mathbf{u}_{i+1})$
Step 8: Increment *i* by 1
Step 9: Exit
where $\mathbf{B} \equiv \mathbf{E}^T\mathbf{E} + \mu\mathbf{I}$, $\mathbf{C} \equiv \mathbf{B}^{-1}\mathbf{1}(\mathbf{1}^T\mathbf{B}^{-1}\mathbf{1})^{-1}$ and λ is a parameter controlling the relative weight. (Note: the symbol ≡ means "is defined as" or "equivalence"). Soft threshold function is discussed in [16].

E. CSUnSAL Total Variation (CSUnSAL TV)

While sparse unmixing techniques characterize mixed pixel problems using spectral libraries, they do not deal with the neighboring pixels and tend to ignore the spatial context. SUnSAL and Total Variation (SUnSAL TV) [17] takes into account spatial information (the relationship between each pixel vector and its neighbors) on the sparse unmixing formulation by means of the TV regularizer [18] assuming that it is very likely that two neighboring pixels have similar fractional abundances for the same endmember. The TV regularizer acts as *a priori* information and unmixing is achieved by a large nonsmooth convex optimization problem. For detailed solution to this optimization problem, readers can refer the Appendix of [17]. SUnSAL TV with ANC and ASC imposed is referred as CSUnSAL TV.

IV. Data

A. Computer simulations

Simulation of imagery was carried out with a set of global spectra of the three endmember libraries [19] to generate three abundance maps. Equation (1) was inverted (with ANC and ASC imposed) to generate computer simulated noise free data of 6 bands of size 512 x 512. In a separate set of experiments, error in the estimate was examined as the noise power (variance) was set to 2, 4, 8, 16, 32, 64, 128 and 256. This noise is a random number drawn from Gaussian distribution where the mean of each endmember is set to 0 and the variability is controlled i.e., Gaussian noise = mean + random perturbation; random perturbation is a Gaussian random variable of specific variance.

B. Landsat data

A spectrally diverse collection of 11 scenes of Level 1 terrain corrected, cloud free Landsat-5 16 bit (path 43, row 35) of Fresno were used in this study. These data were captured on April 4 and 20, May 22, June 7 and 23, July 9 and 25, August 26, September 11 and 27 and October 13 for the year 2008 and were calibrated to exoatmospheric reflectance [20]. Corresponding to the above scenes, a coincidental set of ground canopy cover were available for a number of surveyed field within the footprint of Landsat WRS path 43, row 35 [21]. LEDAPS atmospheric correction method [22] was used to convert atmospheric reflectance to surface reflectance which reduced the perturbations caused by Rayleigh scattering and the absorption of the mixing atmospheric molecules and aerosols. 74 surveyed field polygons of the fractional vegetation cover were generated from digital photographs taken with a multispectral camera mounted on a frame at nadir view pointed 2.3 m above the ground at the commercial agricultural fields of San Joaquin Valley (in central California) on 11 dates mentioned above, except for one date when the Landsat acquisition preceded the ground observation by one day. For each date, 2-4 evenly spaced pictures were taken for an area of 100 m x 100 m with center location marked by a GPS [21]. These fractional measurements belonged to a diverse set of seasonal and perennial crops in various developmental stages, from emergence to full canopy representing an agricultural scenario in the RS data.

A second set of a pair of coincident clear sky Landsat TM-5 data and WV-2 data for an area of San Francisco (SF) were used to assess the algorithms. SF is chosen for the test site because of its urbanized landscape, having colonial and eclectic mix of building architectures on the steep rolling hills. WV-2 data were acquired a few minutes after the Landsat-5 TM data acquisition on May 1, 2010 for an area near the Golden Gate Bridge, SF. The spectral range of the first four bands of Landsat data correspond with the WV-2 bands 2, 3, 5 and 7 in terms of the wavelength range so they have a similar mixing space. WV-2 data were converted to Top of Atmosphere (TOA) Reflectance values using the python program [23] in GRASS GIS 7.1. The Landsat unmixed images were compared with the corresponding WV-2 fraction images for accuracy assessment.

C. Endmember generation

Global mixing spaces using a spectrally diverse LC and diversity of biomes with 100 Landsat ETM+ scenes was used to define a standardized set of spectral endmembers of substrate ("S" – endmember 1 or E1), vegetation ("V" – endmember 2 or E2), and dark objects ("D" – endmember 3 or E3) [24]. Vegetation refers to green photosynthetic plants, dark objects encompass absorptive substrate materials, clear water, deep shadows, etc., and substrate includes soils, sediments, rocks, and non-photosynthetic vegetation. The S-V-D endmember coefficients, with dates and locations of each subscene are available at [25]. The estimates obtained from the global endmembers have been compared to fractional vegetation cover derived vicariously by linearly unmixing near-coincidental WV-2 acquisitions over a set of diverse coastal environments, using both global endmembers and image-specific endmembers to unmix the WV-2 images. The strong 1:1 linear correlation between the fractions obtained from the two types of images indicates that the mixture model fractions scale linearly from 2 m to 30 m over a wide range of terrains. When endmembers are derived from a large enough sample of radiometric responses to encompass the Landsat spectral mixing space, they can be used to build a standardized spectral mixture model with global applicability [26]. UCLS, SCLS, FCLS and MFCLS were implemented in C++ programming language with OpenCV and boost C++ libraries. SPU and SUnSAL programs were obtained from the authors. GRASS GIS was used for visualization of results and statistical analysis was carried in R statistical package on the NASA Earth Exchange [27]. The parameter λ in CSUnSAL was set to 0, in CSUnSAL TV was set to 0.0005, and λ_{TV} in

ISBN: 978-988-14047-2-5
ISSN: 2078-0958 (Print); ISSN: 2078-0966 (Online)

CSUnSAL TV was set to 0.005 for computer simulated data and 0.001 for Landsat data. Here, the maximum number of iterations was set to 100 and all other parameters were set to default. For validation of computer simulated data, the estimated class proportion maps were compared with the synthetic true abundance maps using visual checks and various other measures such as descriptive statistics (minimum and maximum fractional estimates), cc, RMSE and probability of success (p_s). Considering the true abundance $\boldsymbol{\alpha}$ and estimated abundance $\hat{\boldsymbol{\alpha}}$, cc (or r) between $\boldsymbol{\alpha}$ and $\hat{\boldsymbol{\alpha}}$ ranges from –1 to 1, where 1 implies that a linear equation describes the relationship between $\boldsymbol{\alpha}$ and $\hat{\boldsymbol{\alpha}}$ perfectly with all the data points lying on a straight line for which $\hat{\boldsymbol{\alpha}}$ increases as $\boldsymbol{\alpha}$ increases. $r = -1$ infers that all data points lie on a line for which $\hat{\boldsymbol{\alpha}}$ decreases as $\boldsymbol{\alpha}$ increases and $r = 0$ means there is no linear correlation between the true and estimated abundances. On the other hand, a smaller RMSE indicates a better unmixing result i.e. higher accuracy. p_s is an estimate of the probability that the relative error power is smaller than a certain threshold [12] i.e. $p_s \equiv P(\frac{\|\hat{\alpha}-\alpha\|^2}{\|\alpha\|^2} \leq \text{threshold})$. If threshold is 10, and $p_s = 1$, it suggests that the total relative error power of proportional abundances is less than 1/10 with a probability of 1. Estimation result is accepted when $\frac{\|\hat{\alpha}-\alpha\|^2}{\|\alpha\|^2} \leq 0.95$ (5.22 dB). 0.95 is the average of the 99th percentile of all the abundances of the three endmembers for noise variance 8. At this noise variance, the signal-to-noise ratio which is the logarithm to the base 10 of the ratio of sum of the square of the true abundances to the sum of the square of the difference between the estimated and the true abundances turns out to be 5.22 dB. Empirically, we found that when $p_s = 1$, then 1 dB ≤ the SNR for the entire abundance pixels ≤ 8 dB for our data set.

V. Experimental Results and Discussion

A. Computer simulated data

Fig. 1 (a-c) shows noise free synthetic abundance maps for endmember 1, 2 and 3, (d-f) shows estimated abundance maps obtained for each signature class (E1, E2 and E3) corresponding directly to the gray scale values from FCLS, (g-i) from SPU, and (j-l) from CSUnSAL with the range of abundance fraction values specified in square bracket [minimum abundance value – maximum abundance value] underneath each figure. Visual examination of the abundance maps revealed that they were similar in terms of the relative fractions. Table I reveals that for the noise free data, all models have high cc, low RMSE and $p_s = 1$. At noise variance 256, FCLS showed highest cc for endmember 1, followed by MFCLS, SPU and CSUnSAL. All these four methods showed similar cc for endmember 2 and 3. RMSE for these methods were similar for the second and third endmembers and they produced high p_s (0.92). On the other hand, CSUnSAL TV had the worst performance with lowest cc, highest RMSE for all the endmembers and lowest p_s. Note that CSUnSAL TV did not detect endmember 3 with noise variance 256. The details of other noise variances are omitted due to space constraints. For each endmember, all the models showed high cc (close to 1) when variance in the noise was increased till 32, beyond which cc gradually decreased and reached a minimum of 0.12 for endmember 3 for CSUnSAL TV. To a certain noise level (noise variance 32), all the models are robust, however as noise increased in the data, they tend to produce higher RMSE following a hyperbolic curve. FCLS was robust till noise 128. Up to noise variance 16, all the algorithms had $p_s = 1$, beyond which it decreased to 0.46 for CSUnSAL TV for which the quantification results were worse.

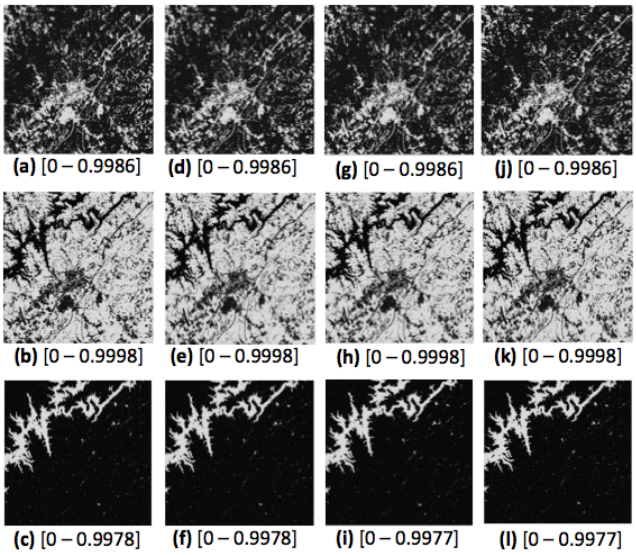

Fig. 1. (a - c) synthetic abundance maps for endmember 1-2-3; abundance maps: (d – f) from FCLS, (g – i) from SPU, and (j – l) from CSUnSAL from noise free data. In the figure, black indicates absence of a particular class (the minimum abundance value) and white indicates full presence of that class in a pixel (the maximum abundance value). Intermediate values of the shades of gray represent mixture of more than one class in a pixel.

TABLE I. CC, RMSE AND p_s FOR ENDMEMBER 1, 2 AND 3 (E1, E2 AND E3) FOR NOISE VARIANCE 0 AND 256

Models	*cc*			RMSE			p_s
	E1	E2	E3	E1	E2	E3	
Noise $\sigma^2 = 0$							
FCLS	1	1	1	0	0	0	1
MFCLS	1	1	1	0	0	0	1
SPU	1	1	1	0	0	0	1
CSUnSAL	1	1	1	0	0	0	1
CSUnSAL TV	1	1	0.99	0	0	0	1
Noise $\sigma^2 = 256$							
FCLS	0.99	0.87	0.81	0.03	0.20	0.15	0.92
MFCLS	0.74	0.87	0.83	0.26	0.20	0.14	0.92
SPU	0.74	0.87	0.83	0.26	0.20	0.14	0.92
CSUnSAL	0.74	0.87	0.83	0.26	0.20	0.14	0.92
CSUnSAL TV	0.32	0.42	0.12	0.89	0.90	64.6	0.46

B. Landsat data – an agricultural landscape

Each of the 11 Landsat scene was unmixed with S-V-D endmembers (E1, E2 and E3) using different models to obtain the abundance estimates. For each scene, the proportions of vegetation fraction were compared with the ground observations. Mean absolute error (MAE) of vegetation fraction for FCLS, MFCLS, SPU and CSUnSAL was 0.08 and for CSUnSAL TV was 0.3. Cc (statistically significant at 0.99 confidence level, *p-value* < 2.2e^{-16}) between ground vegetation fractions and abundance

ISBN: 978-988-14047-2-5
ISSN: 2078-0958 (Print); ISSN: 2078-0966 (Online)

estimates from FCLS, MFCLS, SPU and CSUnSAL were 0.98 and for CSUnSAL TV was 0.21. This indicates that the four constrained models were able to accurately reproduce the proportions of vegetation endmember in the 11 scenes under investigation with similar accuracies.

C. *Landsat data – an urban scenario*

Landsat data of SF (Fig. 2) were unmixed with S-V-D endmembers using the five models. WV-2 data were also unmixed with the same S-V-D endmembers using FCLS algorithm for validating the Landsat abundance maps. FCLS was selected for unmixing WV-2 data since it was robust against noise in synthetic data analysis and performed well in vegetation classification with Landsat data. The WV-2 fractions were convolved with a Gaussian low pass filter having 30 m full width half maximum, with the point spread function of the Landsat sensor and resampled to 30 m.

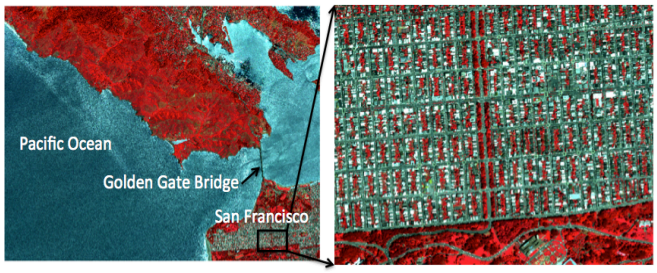

Fig. 2. False colur composite (FCC) of San Francisco in Landsat resolution.

Coordinate comparison of WV-2 and Landsat data sets at many random pixels did not reveal any systematic image registration error. Comparison of Landsat S-V-D fractions to WV-2 S-V-D fractions revealed that MAE of S-V-D fractions for FCLS, MFCLS, SPU and CSUnSAL were 0.09, 0.07 and 0.06, and for CSUnSAL TV were 0.11, 0.07 and 2. Cc of S-V-D fractions for FCLS, MFCLS, SPU and CSUnSAL were 0.87, 0.88 and 0.63 whereas cc for CSUnSAL TV were 0.85, 0.88 and -0.03; CSUnSAL TV was not able to discriminate the dark objects class. The outcome of this study clearly indicates that the constrained models can be used to identify, quantify and estimate materials from the large repository of Landsat data. They are best to assess state, distribution and quantification of materials for spatial-temporal information extraction. Considering the various measures of performance discriminators in the above analysis, FCLS, MFCLS, SPU and CSUnSAL had equally high performance whereas CSUnSAL TV performed worst. Future study of the models with hyperspectral data and numerous endmembers may reveal additional differences between the algorithm's performances.

REFERENCES

[1] A. Plaza, Q. Du, J. M. Bioucas-Dias, X. Jia, and F. Kruse, "Foreword to the special issue on spectral unmixing of remotely sensed data," *IEEE Trans. Geosci. Remote Sens.*, vol. 49, no. 11, pp. 4103–4110, 2011.

[2] M-D. Iordache, J. M. Bioucas-Dias and A. Plaza, "Collaborative Sparse Regression for Hyperspectral Unmixing," *IEEE Trans. Geosci. Remote Sens.*, vol. 52, no. 1, pp. 341–354, 2014.

[3] E. M. Winter, "N-FINDR: An algorithm for fast autonomous spectral end-member determination in hyperspectral data," *in Proc. SPIE*, 1999, vol. 3753, pp. 266-275.

[4] A. Plaza, P. Martinez, R. Perez, and J. Plaza, "A quantitative and comparative analysis of endmember extraction algorithms from hyperspectral data," *IEEE Trans. Geosci. Remote Sens.*, vol. 42, no. 3, pp. 650–663, 2004.

[5] U. Kumar, S. Kumar Raja, C. Mukhopadhyay, and T. V. Ramachandra, "A Neural Network Based Hybrid Mixture Model to Extract Information from Non-linear Mixed Pixels," *Information*, vol. 3, no. 3, pp. 420–441, 2012.

[6] K. Arai, "Non-linear mixture model of mixed pixels in remote sensing satellite images based on Monte Carlo simulation," *Advances in Space Res.*, vol. 42, pp. 1715–1723, 2008.

[7] C.-I Chang, *Hyperspectral Imaging Techniques for Spectral Detection and Classification*. New York: Kluwer Academic / Plenum Publishers, 2003.

[8] J. M. Bioucas-Dias, A. Plaza, N. Dobigeon, M. Parente, Q. Du, P. Gader, and J. Chanussot, "Hyperspectral Unmixing Overview: Geometrical, Statistical, and Sparse Regression-Based Approaches," *IEEE J. Selected Topics Applied Earth Obs. Remote Sens.*, vol. 5, no. 2, pp. 354–379, 2012.

[9] Y. E. Shimabukuro, and A. J. Smith, "The least-squares mixing models to generate fraction images derived from remote sensing multispectral data," *IEEE Trans. Geosci. Remote Sens.*, vol. 29, no. 1, pp. 16–20, 1991.

[10] C. L. Lawson, and R. J. Hanson, *Solving Least Squares Problems*. Philadelphia, PA: SIAM, 1995.

[11] R. Heylen, D. Burazerovi´c, and P. Scheunders, "Fully Constrained Least Squares Spectral Unmixing by Simplex Projection," *IEEE Trans. Geosci. Remote Sens.*, vol. 49, no. 11, pp. 4112–4122, 2011.

[12] M-D. Iordache, J. M. Bioucas-Dias, and A. Plaza, "Sparse Unmixing of Hyperspectral Data," *IEEE Trans. Geosci. Remote Sens.*, vol. 49, no. 6, pp. 2014–2039, 2011.

[13] J. Eckstein, and D. Bertsekas. "On the Douglas-Rachford splitting method and the proximal point algorithm for maximal monotone operators," *Math. Prog.*, vol. 5, pp. 293–318, 1992.

[14] D. Gabay, and B. Mercier, "A dual algorithm for the solution of non-linear variational problems via finite-element approximations," *Comp. Math. with App.*, vol. 2, pp. 17–40, 1976.

[15] J. M. Bioucas-Dias, and M. A. T. Figueiredo, "Alternating direction algorithms for constrained sparse regression: Application to hyperspectral unmixing," *in Proc. of the 2nd Workshop on Hyperspectral Image and Signal Processing: Evolution in Remote Sensing (WHISPERS)*, 14–16 June 2010, vol. 1, no. 4, pp. 14–16, 2010.

[16] S. Chen, D. Donoho, and M. Saunders, "Atomic decomposition by basis pursuit," *SIAM review*, vol. 43, no. 1, pp. 129–159, 1995.

[17] M. D. Iordache, J. M. Bioucas-Dias, and A. Plaza, "Total Variation Spatial Regularization for Sparse Hyperspectral Unmixing," *IEEE Trans. Geosci. Remote Sens.*, vol. 50, no. 11, pp. 4484–4502, 2012.

[18] A. Chambolle, "An algorithm for total variation minimization and applications," *J. Math. Imaging Vis.*, vol. 20(1/2), pp. 89–97, 2004.

[19] http://www.ldeo.columbia.edu/~small/GlobalLandsat/styled-3/index.html [Last accessed: 06 April, 2015. 03:10 pm.]

[20] G. Chander, B. L. Markham, and D. L. Helder, "Summary of current radiometric calibration coefficients for Landsat MSS, TM, ETM+, and EO-1 ALI sensors," *Remote Sens. Env.*, vol. 113, pp. 893–903, 2009.

[21] L. Johnson, and T. Trout, "Satellite-assisted monitoring of vegetable crop evapotranspiration in California's San Joaquin Valley," *Remote Sens.*, vol. 4, pp. 439–455, 2012.

[22] J. G. Masek, E. F. Vermote, N. Saleous, R. Wolfe, F. G. Hall, F., Huemmrich, F. Gao, J. Kutler and T. K. Lim, "A Landsat surface reflectance data set for North America, 1990-2000," *IEEE Geosci. Remote Sens. Letters*, vol. 3, no. 1, pp. 68–72, 2006.

[23] https://github.com/egoddard/i.wv2.toar [Last accessed: 06 April, 2015. 03:15 pm.]

[24] C. Small, and C. Milesi, "Multi-scale Standardized Spectral Mixture Models," *Remote Sens. Env.*, vol. 136, pp. 442–454, 2013.

[25] http://www.LDEO.columbia.edu/~small/GlobalLandsat/ [Last accessed: 06 April, 2015. 03:16 pm.]

[26] C. Small, "The Landsat ETM plus spectral mixing space," *Remote Sens. Env.*, vol. 93, pp. 1–17, 2004.

[27] Nemani, R, Votava, P., Michaelis, A., Metlon, F., and Milesi, C., 2011, Collaborative Supercomputing for Global Change Science. Eos, vol. 92, no. 13, pp. 109 –116.

ISBN: 978-988-14047-2-5
ISSN: 2078-0958 (Print); ISSN: 2078-0966 (Online)